

April 24th 2025

Calcium isotope constraints on Mesoarchean seawater

Anne-Sofie C. Ahm^{1,3}, Philip Fralick², and John A. Higgins³

¹School of Earth and Ocean Sciences, University of Victoria; Victoria BC, V8W 2Y2, Canada.

²Department of Geology, Lakehead University; Thunder Bay ON, P7B 5E1, Canada.

³Department of Geosciences, Princeton University; Princeton NJ, 08544, USA.

This is a non-peer reviewed preprint submitted to EarthArXiv. The manuscript is currently submitted for review in Geology. Please note that following peer-review, subsequent versions of this paper may have slightly different content.

Please address correspondence to Anne-Sofie C. Ahm
Email address: annesofieahm@uvic.ca

1 Calcium isotope constraints on Mesoarchean seawater

2 **Anne-Sofie C. Ahm^{1,3}, Philip Fralick², and John A. Higgins³**

3 *¹School of Earth and Ocean Sciences, University of Victoria; Victoria BC, V8W 2Y2, Canada.*

4 *²Department of Geology, Lakehead University; Thunder Bay ON, P7B 5E1, Canada.*

5 *³Department of Geosciences, Princeton University; Princeton NJ, 08544, USA.*

6

7 **ABSTRACT**

8 The cause of the Great Oxidation Event ~2.4 billion-years-ago (Ga) is hotly debated.
9 Recent models favor the emergence of continents as driving the event. However, we suggest that
10 extensive shallow-marine carbonate platforms existed in the Mesoarchean. This conclusion is
11 based on Ca isotopes from 2.8 Ga carbonate rocks, that constrains the Ca isotope value of
12 Mesoarchean seawater to -0.5‰ relative to present day values. This estimate is strikingly similar
13 to pre-Mesozoic values, suggesting that continental freeboard and the area of carbonate
14 platforms was relatively consistent through most of Earth history. Shallow-marine environments
15 were not only extensive in the Mesoarchean, but carbonate Ce anomalies and Mn concentrations
16 indicate that sedimentary conditions for organic carbon burial existed prior to the rise of
17 atmospheric oxygen.

18

19 **INTRODUCTION**

20 Atmospheric oxygen first rose during the Great Oxygenation Event (GOE) ~2.4 Ga.
21 Recent models suggest that growth in the crustal carbonate reservoir or continental freeboard
22 could have driven the GOE (Alcott et al., 2024; Bindeman et al., 2018; Kump and Barley, 2007).
23 These models propose that cyanobacteria capable of oxygenic photosynthesis were limited in

24 extent by suitable available areas, low nutrient inputs from the lack of continental weathering, or
25 that the reductant input to the atmosphere from submarine volcanism exceeded O₂ production
26 rates. However, the cause of the GOE is debated due to the lack of robust geochemical records,
27 as Archean sedimentary rocks all have been significantly altered (Planavsky et al., 2010; Slotznick
28 et al., 2022).

29 We provide a framework to interpret geochemical signals in Archean carbonate rocks by
30 disentangling the effects of diagenesis from primary seawater signatures using Ca isotope
31 ($\delta^{44}\text{Ca} = \left(\frac{{}^{44}\text{Ca}_{\text{sample}}}{{}^{44}\text{Ca}_{\text{modern seawater}}} - 1 \right) * 1000$). This framework relies on the
32 sensitivity of $\delta^{44}\text{Ca}$ values and ratios of Sr/[Ca+Mg] to carbonate mineralogy (aragonite, calcite,
33 dolomite) and diagenesis (Ahm et al., 2018; Fantle and Higgins, 2014; Higgins et al., 2018). The
34 sensitivity of carbonate $\delta^{44}\text{Ca}$ values to diagenesis is a consequence of the rate dependence of
35 isotope fractionation (ϵ) (Tang et al., 2008), resulting in the preferential incorporation of the
36 lighter isotope into carbonate minerals at higher precipitation rates. Primary carbonates that form
37 relatively fast in the surface ocean are fractionated relative to seawater: $\epsilon \sim -1.4\text{‰}$ and -1.1‰ for
38 aragonite and calcite, respectively (Gussone et al., 2005). However, during diagenesis slow rates
39 associated with carbonate recrystallization result in little to no fractionation relative to the pore-
40 fluid (Fantle and DePaolo, 2007). A complimentary behavior is observed for Sr/[Ca+Mg] ratios
41 where aragonite is enriched in Sr relative to early diagenetic calcite or dolomite (Tang et al.,
42 2008).

43 Here we use $\delta^{44}\text{Ca}$ values and Sr/[Ca+Mg] ratios to parse the diagenetic history of
44 Mesoarchean carbonate rocks into three different stages: The first stage of diagenesis occurs
45 immediately below the seafloor. In this setting, sediment pore-fluids are buffered by seawater
46 such that the geochemistry of pore-filling and replacement fabrics tend to track coeval seawater.

47 Early-diagenetic seawater-buffered fabrics will have elevated $\delta^{44}\text{Ca}$ values combined with low
48 $\text{Sr}/[\text{Ca}+\text{Mg}]$ ratios (Higgins et al., 2018).

49 The second stage of diagenesis occurs during intermediate burial. At this stage, the
50 porosity and permeability has been reduced and the chemistry of pore-fluids is buffered by
51 partial dissolution of sediments. The diagenetic replacement fabrics that form here will preserve
52 the $\delta^{44}\text{Ca}$ values of the dissolving (primary) sediment. For example, while primary aragonite may
53 undergo recrystallization to calcite, at this stage they will preserve the low $\delta^{44}\text{Ca}$ values that are
54 diagnostic for aragonite. Similarly, relatively high $\text{Sr}/[\text{Ca}+\text{Mg}]$ ratios will be retained, reflecting
55 the sediment-buffered pore-fluid environment. Sediments that are stabilized during this
56 intermediate stage of diagenesis are most likely to preserve $\delta^{44}\text{Ca}$ (and $\delta^{13}\text{C}$) values of the
57 primary carbonate, while more sensitive proxies like $\delta^{18}\text{O}$ still can be reset.

58 Finally, diagenesis can continue to occur during late-stage burial. At this stage,
59 temperatures and pressures are high and late-stage fabrics may form in reaction with crustal
60 fluids. While the composition of these fabrics will depend on the crustal fluid, low $\text{Sr}/[\text{Ca}+\text{Mg}]$
61 ratios and $\delta^{44}\text{Ca}$ values approaching Bulk Silicate Earth (BSE) $\sim -0.96\text{‰}$ are expected (Skulan et
62 al., 1997). Sediments that are stabilized during this late stage of diagenesis are unlikely to reflect
63 primary seawater chemistry.

64 By targeting carbonate end-members from early-diagenetic calcite cements to modified
65 “primary” aragonite, it is possible to estimate $\delta^{44}\text{Ca}$ value of ancient seawater. The prediction is
66 that these two end-members should offer independent, but consistent, records of seawater
67 confirmed by a $\delta^{44}\text{Ca}$ offset of $\sim 1.4\text{‰}$ between the sediment-buffered “primary aragonite” and
68 fluid-buffered calcite cements, and a pronounced co-variance between $\text{Sr}/[\text{Ca}+\text{Mg}]$ and $\delta^{44}\text{Ca}$.
69 Critically, the range in $\delta^{44}\text{Ca}$ values that results from the different stages of diagenesis is larger

70 (>1‰) than plausible changes in seawater $\delta^{44}\text{Ca}$ values resulting from transient perturbations in
71 the global Ca cycle ($\ll 1\%$) (Komar and Zeebe, 2016).

72 We apply this Ca isotope framework to ~ 2.8 Ga carbonate rocks (Tomlinson et al., 2003)
73 from the Mosher Formation, Ontario, by measuring fabric specific $\delta^{44}\text{Ca}$ values, combined with
74 $\delta^{13}\text{C}$ and $\delta^{18}\text{O}$ values, elemental concentrations, and rare earth element patterns (REE+Y). The
75 geochemistry of the Mosher carbonate is well characterized by previous studies (Fralick et al.,
76 2024; Fralick and Riding, 2015; Kurucz and Fralick, 2018), but is a center of debate regarding
77 the potential preservation of an Archean oxygen oasis (Planavsky et al., 2010; Riding et al.,
78 2022, 2014). Our results provide new insights by shedding light on the global Ca cycle at 2.8 Ga.

79

80 **RESULTS AND DISCUSSION**

81 The geochemistry of fabric specific samples from the Mosher carbonate can be grouped into
82 three categories: (1) fluid-buffered fabrics, (2) sediment-buffered “primary” fabrics, and (3) late-
83 stage altered fabrics. These three end-members are identified by a combination of their physical
84 appearance, petrographic observations, and geochemical characteristics (Fig. 1).

85 **Fluid-buffered fabrics**

86 Samples classified as fluid-buffered have characteristics consistent with early post-
87 depositional precipitation of carbonate in the sediment pore-space. These samples are
88 predominantly net-like fenestral microbialites or hardgrounds (Fig. 1F,I). The fenestrae consist
89 of low-Mg calcite cements, growing in relatively large (~ 0.5 -5mm) pore-spaces within a
90 microbial framework (Fralick and Riding, 2015). These net-like fabrics are interpreted to have
91 formed prior to sediment compaction, as the microbial pore-space would have collapsed during
92 burial (Sumner, 2000).

93 The $\delta^{44}\text{Ca}$ values of the fluid-buffered fabrics are generally high, up to -0.5‰ (Fig. 1A-
94 D). The $\delta^{13}\text{C}$ values are similarly to calcite formed in the modern ocean (mean, $\mu=1.5\text{‰}$), but
95 with some values reaching as low as -1‰ . $\delta^{18}\text{O}$ values are significantly depleted ($\mu=-9.5\text{‰}$) and
96 are not distinct between different diagenetic phases (Fig. 1D).

97 The fluid-buffered fabrics tend to have intermediate $\text{Mn}/(\text{Ca}+\text{Mg})$ ratios
98 ($\mu=8.3\text{mmol/mol}$) and low ratios of $\text{Sr}/(\text{Ca}+\text{Mg})$ ($\mu=0.1\text{mmol/mol}$) (Fig. 1A-B). They are
99 enriched in heavy relative to the light REEs (Fig. 2B), and some samples contain positive Ce
100 anomalies (up to 2.2), but most do not ($\mu=1.1\pm 0.4$) (Fig. 3B). We interpret these geochemical
101 signatures as consistent with calcite cements precipitating or recrystallizing during early stages
102 of diagenesis, within a reducing pore-space environment.

103 **Sediment-buffered “primary” fabrics**

104 Samples characterized as sediment-buffered preserve some primary geochemical signals
105 and are identified as dark seafloor crystal fans with white sparry calcite or rare pink dolomite
106 infill between individual crystal blades (Fig. 1J). Today, these samples are predominantly low-
107 Mg calcite, but have been interpreted as pseudomorphs after aragonite (Fralick and Riding,
108 2015).

109 The $\delta^{44}\text{Ca}$ values of the sediment-buffered fabrics support an aragonitic origin with low
110 values (down to -1.9‰) correlating with relatively high $\text{Sr}/[\text{Ca}+\text{Mg}]$ ratios up to 1.86mmol/mol
111 (Fig. 1A). The $\delta^{13}\text{C}$ values range between 2.5‰ - 3.0‰ (Fig. 1C). The offset between fluid-buffered
112 cements and pseudomorph aragonite fans is consistent with expectations for aragonite-calcite C
113 isotopic fractionation of $\sim 1.0\text{‰}$ - 1.5‰ (Romanek et al., 1992) and with $\delta^{44}\text{Ca}$ ϵ values $\sim 1.4\text{‰}$
114 (Gussone et al., 2005).

115 The sediment-buffered samples have relatively low Mn/[Ca+Mg] ($\mu=4.9\text{mmol/mol}$).
116 While these ratios are low compared to the other diagenetic endmembers, they are orders of
117 magnitude higher than observed in carbonates across the Bahamas Bank ($\sim 0.04\text{mmol/mol}$)
118 (Higgins et al., 2018), likely indicating much higher concentrations of Mn^{2+} in Mesozoic
119 seawater relative to today (Fig. 1B). REE+Y patterns in sediment-buffered fabrics also have
120 distinct negative Ce anomalies ($\text{Ce/Ce}^* \mu=0.6\pm 0.2$) (Fig. 3A). Finally, despite being well-
121 preserved, the sediment-buffered samples have depleted $\delta^{18}\text{O}$ values that overlap in range with
122 the fluid-buffered and late-stage end-members.

123 **Late-stage diagenetic fabrics**

124 Samples altered by late-stage diagenesis have reacted with crustal fluids during burial under
125 higher temperatures and pressure. These samples are visually identified by significant cross-
126 cutting veins, silicification, and/or ferroan zebra dolomite replacement with saddle-formed
127 crystals (Fig. 1E, H).

128 The late-stage altered samples have $\delta^{44}\text{Ca}$ values approaching BSE and are homogeneous
129 within and across several hand samples ($\mu=-1.04\pm 0.16\text{‰}$) (Fig. 1A-D). They have $\delta^{13}\text{C}$ and $\delta^{18}\text{O}$
130 values spanning a relatively large range depending on the targeted fabrics (Fig. 1C-D). The range
131 in $\delta^{13}\text{C}$ values (-1.9 to 4.3‰) is interpreted to reflect the degree of interaction between the
132 altering crustal fluid and ^{13}C -depleted organic carbon locally within the wall rock. The large
133 range in $\delta^{18}\text{O}$ values (-14.4 to -5.9‰) may reflect partial recrystallization of metastable
134 carbonate minerals during different stages of late-stage alteration.

135 The late-stage alteration samples are also characterized by high ratios of Mn/[Ca+Mg]
136 ($\mu=18.2\text{mmol/mol}$) and low ratios of Sr/[Ca+Mg] ($\mu= 0.07\text{mmol/mol}$) (Fig. 1A-B) and there is a
137 general enrichment in the middle REEs relative to the light and heavy REEs (Fig. 2C). None of

138 the samples categorized as late-stage end-members contain negative Ce/Ce* anomalies
139 ($\mu=1.2\pm0.2$) (Fig. 3A).

140 **The Archean carbonate factory**

141 The geochemical differences between the diagenetic endmembers are consistent with
142 redox-cycling across the ancient seafloor. The sediment-buffered crystal fans that formed above
143 the seafloor contain negative Ce anomalies and low Mn concentrations. In contrast, fluid-
144 buffered microbial fenestral cements that formed within sediments record no or positive Ce
145 anomalies and higher Mn concentrations. To explain these trends, oxidation of soluble Ce³⁺ to
146 insoluble Ce⁴⁺ (and Mn²⁺ to Mn-oxides) must have occurred somewhere in the water column
147 away from where the fans were forming, while reducing conditions persisted in the sediment
148 pore-spaces, driven by the remineralization of organic carbon. This interpretation is also
149 consistent with the lower $\delta^{13}\text{C}$ values ($\sim-1\%$) observed in fenestral net-like cements, relative to
150 values $\sim-2.5\%$ observed in crystal fans (Fig. 1C). These observations imply that organic carbon
151 was buried and partially respired using available oxidants during early diagenesis, driving the
152 dissolution of metastable carbonates similarly to processes in modern marine sediments.

153 The interpretation that early diagenesis was established in Mesoarchean shallow-marine
154 environments is also supported by $\delta^{44}\text{Ca}$ and Sr/[Ca+Mg] ratios. The co-variation observed
155 between $\delta^{44}\text{Ca}$ and Sr/[Ca+Mg] ratios in sediment- and fluid-buffered fabrics is indistinguishable
156 from similar data sets from the Proterozoic and Paleozoic (Gussone et al., 2020), but consistently
157 offset towards lower $\delta^{44}\text{Ca}$ values by $\sim-0.5\%$ compared to modern seawater, providing a
158 constraint on Mesoarchean seawater (Fig. 1A, 3B).

159 The estimated $\delta^{44}\text{Ca}$ value of Mesoarchean seawater provide insight into the extend of
160 shallow water carbonate deposition. Importantly, depleted seawater $\delta^{44}\text{Ca}$ values are not unique

161 to the Mesoarchean, but strikingly similar to the long-term pre-Mesozoic record. For example,
162 low $\delta^{44}\text{Ca}$ values between ~ -1.7 and -2‰ are observed in carbonates from the Neoproterozoic
163 (Ahm et al., 2021, 2019; Busch et al., 2022), Ordovician (Jones et al., 2020), Silurian (Farkaš et
164 al., 2016), and lower Triassic (Lau et al., 2017). While there is variability in these records caused
165 by changes in primary mineralogy and diagenesis, the low $\delta^{44}\text{Ca}$ values are unique to the pre-
166 Mesozoic and do not reappear in the Cenozoic. These observations imply that, on average,
167 seawater $\delta^{44}\text{Ca}$ remained approximately $\sim -0.5\text{‰}$ lower relative to today from the Mesoarchean
168 until the advent of pelagic calcification in the Mesozoic.

169 A simple mass balance approach can be used to understand the consequences of the
170 reconstructed seawater $\delta^{44}\text{Ca}$ value for the global Ca and C cycle. The main source of Ca to the
171 ocean is weathering inputs with an average $\delta^{44}\text{Ca}$ value matching BSE, -0.96‰ (Blättler and
172 Higgins, 2017). The dominant Ca sink is deposition of carbonate sediments. While the ϵ value
173 between carbonate and seawater can have a wide range, on long time-scales the bulk carbonate
174 sink must have an average $\delta^{44}\text{Ca}$ value matching weathering inputs. For example, for
175 Mesoarchean seawater to have a value of -0.5‰ relative to today, the average ϵ value of the bulk
176 carbonate sink must have been $\sim -0.5\text{‰}$. This isotope effect is about half the size of the ϵ value
177 between seawater and bulk carbonate sediments observed today ($\sim 1\text{‰}$) (Gussone et al., 2020).

178 Since hypothetical deep marine carbonates (e.g., microbially mediated or abiotic seafloor
179 fans) would have formed in low fluid-flow environments, their $\delta^{44}\text{Ca}$ value would tend to be
180 sediment-buffered and thus be too isotopically depleted to balance the Mesoarchean carbonate
181 budget. That leaves two options for a Mesoarchean bulk carbonate sink with an isotope effect of
182 $\sim -0.5\text{‰}$: (1) Shallow marine carbonate platforms or (2) carbonate veins in ocean crust (Bjerrum
183 and Canfield, 2004). Previous studies have shown that early marine diagenesis and

184 dolomitization is a dominant process in carbonate platforms resulting in values ~ -0.5 to -0.3%
185 for this sink (Higgins et al., 2018). For carbonate veins in ocean crust, the average $\delta^{44}\text{Ca}$ value is
186 not well known and a wide range have been reported (Amini et al., 2008; Blättler and Higgins,
187 2017). The average value of vein carbonates is, however, broadly bound by observations that the
188 average $\delta^{44}\text{Ca}$ value of platform carbonate has been equal to BSE and invariant since the
189 Archean. If carbonate veins were a significant sink with elevated $\delta^{44}\text{Ca}$ values (relative to BSE),
190 mass balance requires that the average platform carbonate value would evolve to be lighter than
191 BSE. Since this effect is not observed (Blättler and Higgins, 2017), we suggest that the low $\delta^{44}\text{Ca}$
192 value of Mesoarchean seawater likely is a result of widespread deposition of carbonate platform
193 sediments (Fralick et al., 2025).

194

195 **CONCLUSION**

196 We suggest that the Mesoarchean carbonate factory was dominated by shallow-water
197 carbonate platforms, similar to the Proterozoic and the Phanerozoic, prior to the rise of pelagic
198 calcifiers. Together with observations of active sedimentary redox-cycling, these results suggest
199 that shallow-marine environments favorable for organic carbon burial were widespread and
200 question whether an expansion of shallow marine areas at ~ 2.4 Ga is the root cause of the GOE.

201

202 **ACKNOWLEDGMENTS**

203 This work was supported by a grant from the Simons Foundation (SCOL 611878, ASCA)
204 and by the Natural Science and Engineering Research Council of Canada (NSERC) Discovery
205 Grant to ASCA (RFPIN-2022-03912) and Discovery Grant to PF.

206

207 REFERENCES CITED

- 208 Ahm, A.-S.C., Bjerrum, C.J., Blättler, C.L., Swart, P.K., Higgins, J.A., 2018. Quantifying early
209 marine diagenesis in shallow-water carbonate sediments. *Geochim. Cosmochim. Acta*
210 236, 140–159. <https://doi.org/10.1016/j.gca.2018.02.042>
- 211 Ahm, A.-S.C., Bjerrum, C.J., Hoffman, P.F., Macdonald, F.A., Maloof, A.C., Rose, C.V.,
212 Strauss, J.V., Higgins, J.A., 2021. The Ca and Mg isotope record of the Cryogenian
213 Trezona carbon isotope excursion. *Earth Planet. Sci. Lett.* 568, 117002.
214 <https://doi.org/10.1016/j.epsl.2021.117002>
- 215 Ahm, A.-S.C., Maloof, A.C., Macdonald, F.A., Hoffman, P.F., Bjerrum, C.J., Bold, U., Rose,
216 C.V., Strauss, J.V., Higgins, J.A., 2019. An early diagenetic deglacial origin for basal
217 Ediacaran “cap dolostones.” *Earth Planet. Sci. Lett.* 506, 292–307.
218 <https://doi.org/10.1016/j.epsl.2018.10.046>
- 219 Alcott, L.J., Walton, C., Planavsky, N.J., Shorttle, O., Mills, B.J.W., 2024. Crustal carbonate
220 build-up as a driver for Earth’s oxygenation. *Nat. Geosci.* 1–7.
221 <https://doi.org/10.1038/s41561-024-01417-1>
- 222 Amini, M., Eisenhauer, A., Böhm, F., Fietzke, J., Bach, W., Garbe-Schönberg, D., Rosner, M.,
223 Bock, B., Lackschewitz, K.S., Hauff, F., 2008. Calcium isotope ($\delta^{44}\text{Ca}$) fractionation
224 along hydrothermal pathways, Logatchev field (Mid-Atlantic Ridge, 14°45’N). *Geochim.*
225 *Cosmochim. Acta* 72, 4107–4122. <https://doi.org/10.1016/j.gca.2008.05.055>
- 226 Bindeman, I.N., Zakharov, D.O., Palandri, J., Greber, N.D., Dauphas, N., Retallack, G.J.,
227 Hofmann, A., Lackey, J.S., Bekker, A., 2018. Rapid emergence of subaerial landmasses
228 and onset of a modern hydrologic cycle 2.5 billion years ago. *Nature* 557, 545–548.
229 <https://doi.org/10.1038/s41586-018-0131-1>
- 230 Bjerrum, C.J., Canfield, D.E., 2004. New insights into the burial history of organic carbon on the
231 early Earth. *Geochem. Geophys. Geosystems* 5. <https://doi.org/10.1029/2004GC000713>
- 232 Blättler, C.L., Higgins, J.A., 2017. Testing Urey’s carbonate–silicate cycle using the calcium
233 isotopic composition of sedimentary carbonates. *Earth Planet. Sci. Lett.* 479, 241–251.
234 <https://doi.org/10.1016/j.epsl.2017.09.033>
- 235 Busch, J.F., Hodgin, E.B., Ahm, A.-S.C., Husson, J.M., Macdonald, F.A., Bergmann, K.D.,
236 Higgins, J.A., Strauss, J.V., 2022. Global and local drivers of the Ediacaran Shuram
237 carbon isotope excursion. *Earth Planet. Sci. Lett.* 579, 117368.
238 <https://doi.org/10.1016/j.epsl.2022.117368>
- 239 Fantle, M.S., DePaolo, D.J., 2007. Ca isotopes in carbonate sediment and pore fluid from ODP
240 Site 807A: The $\text{Ca}^{2+}(\text{aq})$ –calcite equilibrium fractionation factor and calcite
241 recrystallization rates in Pleistocene sediments. *Geochim. Cosmochim. Acta* 71, 2524–
242 2546. <https://doi.org/10.1016/j.gca.2007.03.006>
- 243 Fantle, M.S., Higgins, J., 2014. The effects of diagenesis and dolomitization on Ca and Mg
244 isotopes in marine platform carbonates: Implications for the geochemical cycles of Ca
245 and Mg. *Geochim. Cosmochim. Acta* 142, 458–481.
246 <https://doi.org/10.1016/j.gca.2014.07.025>
- 247 Farkaš, J., Frýda, J., Holmden, C., 2016. Calcium isotope constraints on the marine carbon cycle
248 and CaCO_3 deposition during the late Silurian (Ludfordian) positive $\delta^{13}\text{C}$ excursion.
249 *Earth Planet. Sci. Lett.* 451, 31–40. <https://doi.org/10.1016/j.epsl.2016.06.038>
- 250 Fralick, P., Davis, D.W., Afroz, M., Ramsay, B., Patry, L., Wilmeth, D., Homann, M., Sansjofre,
251 P., Riding, R., Lalonde, S.V., 2025. Earth’s earliest known extensive, thick carbonate

252 platform suggested by new age constraints. *Earth Planet. Sci. Lett.* 656, 119273.
253 <https://doi.org/10.1016/j.epsl.2025.119273>

254 Fralick, P., Himmler, T., Lalonde, S.V., Riding, R., 2024. Localized geochemical variability
255 produced by depositional and diagenetic processes in a 2.8 Ga Ca-carbonate system: A
256 cautionary paradigm. *Precambrian Res.* 410, 107499.
257 <https://doi.org/10.1016/j.precamres.2024.107499>

258 Fralick, P., Riding, R., 2015. Steep Rock Lake: Sedimentology and geochemistry of an Archean
259 carbonate platform. *Earth-Sci. Rev.* 151, 132–175.
260 <https://doi.org/10.1016/j.earscirev.2015.10.006>

261 Gussone, N., Ahm, A.-S.C., Lau, K.V., Bradbury, H.J., 2020. Calcium isotopes in deep time:
262 Potential and limitations. *Chem. Geol.* 544, 119601.
263 <https://doi.org/10.1016/j.chemgeo.2020.119601>

264 Gussone, N., Böhm, F., Eisenhauer, A., Dietzel, M., Heuser, A., Teichert, B.M.A., Reitner, J.,
265 Wörheide, G., Dullo, W.-C., 2005. Calcium isotope fractionation in calcite and aragonite.
266 *Geochim. Cosmochim. Acta* 69, 4485–4494. <https://doi.org/10.1016/j.gca.2005.06.003>

267 Heard, A.W., Bekker, A., Kovalick, A., Tsikos, H., Ireland, T., Dauphas, N., 2022. Oxygen
268 production and rapid iron oxidation in stromatolites immediately predating the Great
269 Oxidation Event. *Earth Planet. Sci. Lett.* 582, 117416.
270 <https://doi.org/10.1016/j.epsl.2022.117416>

271 Higgins, J.A., Blättler, C.L., Lundstrom, E.A., Santiago-Ramos, D.P., Akhtar, A.A., Crüger
272 Ahm, A.-S., Bialik, O., Holmden, C., Bradbury, H., Murray, S.T., Swart, P.K., 2018.
273 Mineralogy, early marine diagenesis, and the chemistry of shallow-water carbonate
274 sediments. *Geochim. Cosmochim. Acta* 220, 512–534.
275 <https://doi.org/10.1016/j.gca.2017.09.046>

276 Jones, D.S., Brothers, R.W., Crüger Ahm, A.-S., Slater, N., Higgins, J.A., Fike, D.A., 2020. Sea
277 level, carbonate mineralogy, and early diagenesis controlled $\delta^{13}\text{C}$ records in Upper
278 Ordovician carbonates. *Geology* 48, 194–199. <https://doi.org/10.1130/G46861.1>

279 Komar, N., Zeebe, R.E., 2016. Calcium and calcium isotope changes during carbon cycle
280 perturbations at the end-Permian. *Paleoceanography* 31, 115–130.
281 <https://doi.org/10.1002/2015PA002834>

282 Kump, L.R., Barley, M.E., 2007. Increased subaerial volcanism and the rise of atmospheric
283 oxygen 2.5 billion years ago. *Nature* 448, 1033–1036.
284 <https://doi.org/10.1038/nature06058>

285 Kurucz, S., Fralick, P., 2018. Internal fabric of giant domes in the Mesoarchean Steep Rock
286 carbonate platform, Superior Province, Canada. *Can. J. Earth Sci.* 55, 343–355.
287 <https://doi.org/10.1139/cjes-2017-0173>

288 Lau, K.V., Maher, K., Brown, S.T., Jost, A.B., Altiner, D., DePaolo, D.J., Eisenhauer, A.,
289 Kelley, B.M., Lehrmann, D.J., Paytan, A., Yu, M., Silva-Tamayo, J.C., Payne, J.L., 2017.
290 The influence of seawater carbonate chemistry, mineralogy, and diagenesis on calcium
291 isotope variations in Lower-Middle Triassic carbonate rocks. *Chem. Geol.* 471, 13–37.
292 <https://doi.org/10.1016/j.chemgeo.2017.09.006>

293 Li, F., Webb, G.E., Algeo, T.J., Kershaw, S., Lu, C., Oehlert, A.M., Gong, Q., Pourmand, A.,
294 Tan, X., 2019. Modern carbonate ooids preserve ambient aqueous REE signatures. *Chem.*
295 *Geol.* 509, 163–177. <https://doi.org/10.1016/j.chemgeo.2019.01.015>

296 Planavsky, N., Bekker, A., Rouxel, O.J., Kamber, B., Hofmann, A., Knudsen, A., Lyons, T.W.,
297 2010. Rare Earth Element and yttrium compositions of Archean and Paleoproterozoic Fe

298 formations revisited: New perspectives on the significance and mechanisms of
299 deposition. *Geochim. Cosmochim. Acta* 74, 6387–6405.
300 <https://doi.org/10.1016/j.gca.2010.07.021>

301 Riding, R., Fralick, P., Liang, L., 2014. Identification of an Archean marine oxygen oasis.
302 *Precambrian Res.* 251, 232–237. <https://doi.org/10.1016/j.precamres.2014.06.017>

303 Riding, R., Liang, L., Fralick, P., 2022. Oxygen-induced chemocline precipitation between
304 Archean Fe-rich and Fe-poor carbonate seas. *Precambrian Res.* 383, 106902.
305 <https://doi.org/10.1016/j.precamres.2022.106902>

306 Romanek, C.S., Grossman, E.L., Morse, J.W., 1992. Carbon isotopic fractionation in synthetic
307 aragonite and calcite: Effects of temperature and precipitation rate. *Geochim.*
308 *Cosmochim. Acta* 56, 419–430. [https://doi.org/10.1016/0016-7037\(92\)90142-6](https://doi.org/10.1016/0016-7037(92)90142-6)

309 Skulan, J., DePaolo, D.J., Owens, T.L., 1997. Biological control of calcium isotopic abundances
310 in the global calcium cycle. *Geochim. Cosmochim. Acta* 61, 2505–2510.
311 [https://doi.org/10.1016/S0016-7037\(97\)00047-1](https://doi.org/10.1016/S0016-7037(97)00047-1)

312 Slotznick, S.P., Johnson, J.E., Rasmussen, B., Raub, T.D., Webb, S.M., Zi, J.-W., Kirschvink,
313 J.L., Fischer, W.W., 2022. Reexamination of 2.5-Ga “whiff” of oxygen interval points to
314 anoxic ocean before GOE. *Sci. Adv.* 8. <https://doi.org/10.1126/sciadv.abj7190>

315 Sumner, D.Y., 2000. Microbial vs Environmental Influences on the Morphology of Late Archean
316 Fenestrate Microbialites, in: Riding, R.E., Awramik, S.M. (Eds.), *Microbial Sediments*.
317 Springer Berlin Heidelberg, Berlin, Heidelberg, pp. 307–314.
318 https://doi.org/10.1007/978-3-662-04036-2_33

319 Tang, J., Dietzel, M., Böhm, F., Köhler, S.J., Eisenhauer, A., 2008. Sr²⁺/Ca²⁺ and 44Ca/40Ca
320 fractionation during inorganic calcite formation: II. Ca isotopes. *Geochim. Cosmochim.*
321 *Acta* 72, 3733–3745. <https://doi.org/10.1016/j.gca.2008.05.033>

322 Tomlinson, K.Y., Davis, D.W., Stone, D., Hart, T.R., 2003. U–Pb age and Nd isotopic evidence
323 for Archean terrane development and crustal recycling in the south-central Wabigoon
324 subprovince, Canada. *Contrib. Mineral. Petrol.* 144, 684–702.
325 <https://doi.org/10.1007/s00410-002-0423-0>

326 Webb, G.E., Kamber, B.S., 2000. Rare earth elements in Holocene reefal microbialites: a new
327 shallow seawater proxy. *Geochim. Cosmochim. Acta* 64, 1557–1565.
328 [https://doi.org/10.1016/S0016-7037\(99\)00400-7](https://doi.org/10.1016/S0016-7037(99)00400-7)

329

330

331

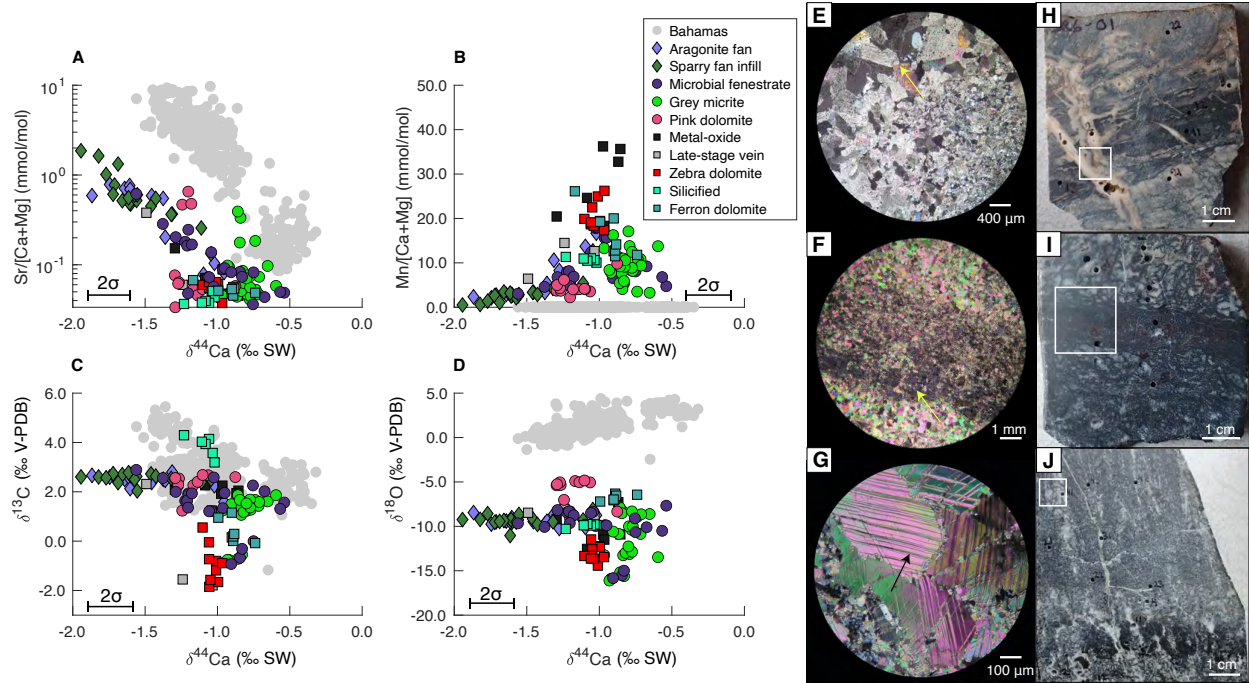
332

333

334

335

336



338

339 **Fig. 1.** Geochemical analysis of sample groups. A-D Sample markers are colored according to
 340 petrographic classification and recent Bahamian carbonate data is included for comparison in
 341 gray (Higgins et al., 2018). E,H late-stage samples include carbonate veins with saddle dolomite
 342 crystals observed in cross-polarized light. The white square in H indicates the approximate area
 343 of the microscope image. F,I fluid-buffered samples include calcite spar infilling open and partly
 344 collapsed microbial fenestrate. G, J “primary” sediment-buffered samples include dark crystal
 345 fans growing from a microbial framework with inter-fan porosity infilled by white calcite spar,
 346 showing twinning and minor silicification.

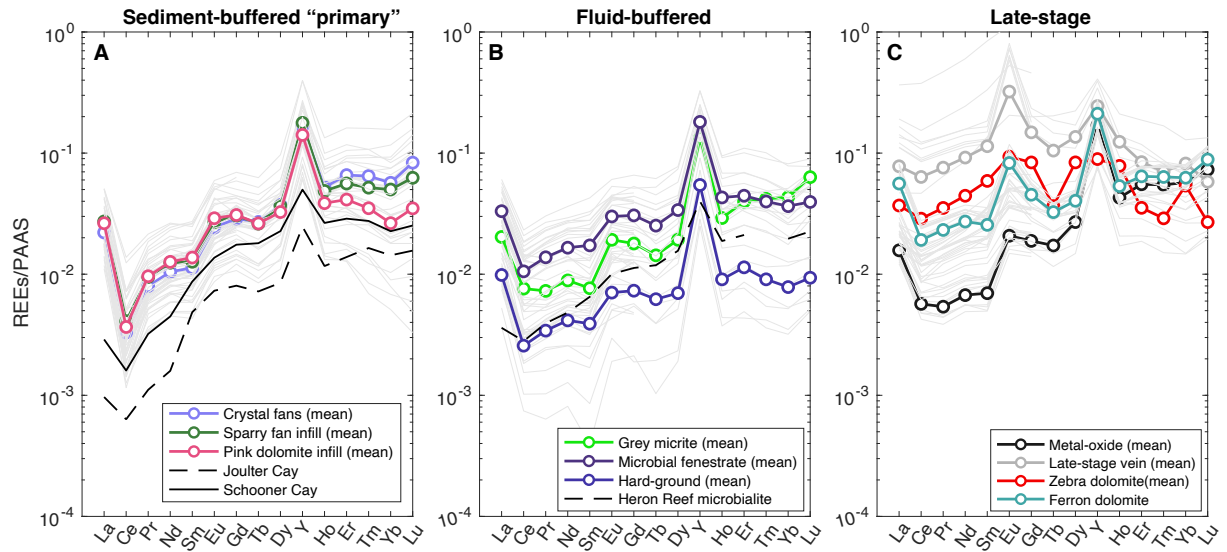
347

348

349

350

351



352

353 **Fig. 2.** REE+Y patterns of the sample groups. Gray lines represent individual measurements of
 354 all samples while colored lines are the mean of several measurements of similar fabrics. REE+Y
 355 patterns of modern Bahamian carbonate sediments (Li et al., 2019) and from a modern microbial
 356 sediment are included (Webb and Kamber, 2000).

357

358

359

360

361

362

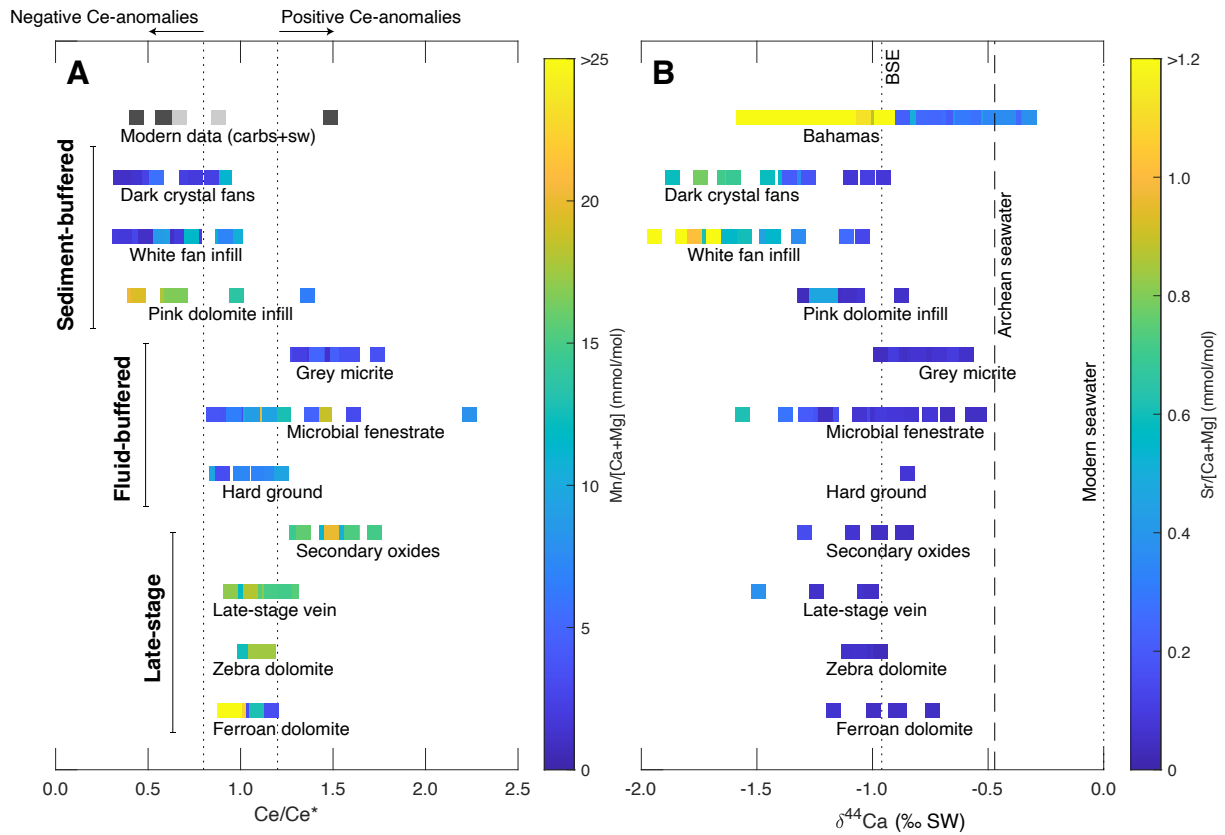
363

364

365

366

367



368

369 **Fig. 3.** Range of Ce anomalies (A) and $\delta^{44}\text{Ca}$ values (A) in carbonate fabrics. Ce/Ce* anomalies
 370 are calculated using the Langrangian formulation (Heard et al., 2022), thereby avoiding
 371 normalization to anomalous La. Measurements of modern carbonate and seawater are shown for
 372 comparison in dark and light gray, respectively (Li et al., 2019). B The $\delta^{44}\text{Ca}$ value of modern
 373 seawater, Bulk Silicate Earth (BSE) and our estimate of Mesoarchean seawater is indicated.

374

375

376

377

378 ¹Supplemental Material. Geological Background and Geochemical Methods, Figures S1-S4,

379 Data file S1. Please visit <https://doi.org/10.1130/XXXX> to access the supplemental material, and

380 contact editing@geosociety.org with any questions.

Supplementary Materials for

Calcium isotope constraints on Mesoarchean seawater

Anne-Sofie C. Ahm^{1,3*}, Philip Fralick², John A. Higgins³

Corresponding author: annesofieahm@uvic.ca

The PDF file includes:

Geological Setting
Methods: Geochemical analysis
Figs. S1 to S4

Other Supplementary Materials for this manuscript include the following:

Data S1: Geochemical data, excel file

MATERIALS AND METHODS

Geological setting

Neoproterozoic metasediments from the Steep Rock Group, including the Mosher Formation, are exposed along the northeastern shorelines of the Steep Rock Lake located 5 km north of Atikokan, Northwestern Ontario (Fig S1) (Fralick and Riding, 2015). The depositional age of the Mosher Formation is constrained by U-Pb zircon ages of the over- and underlying stratigraphic units. The underlying Wagita Formation is composed of discontinuous lenses of conglomerate and sandstone deposited in paleo-channels eroded into the 3001.6±1.7 Ma intrusive Marmion Batholith (Tomlinson et al., 2003). The Mosher Formation is stratigraphically overlain by 400 m of iron formation followed by a pyroclastic komatiite assemblage dated at 2780.4±1.4 Ma, based on the youngest inherited zircons (Tomlinson et al., 2003).

The Mosher Formation consists of dark to light gray limestone and in some locations preserves microbial fenestrate, stromatolites, and crystal fans likely formed in a carbonate platform environment (Fralick and Riding, 2015). Primary sedimentary features, however, are often not discernible due to the complex post-depositional history involving Kenoran greenschist facies metamorphism (~2.7 Ga). In some locations the limestone has experienced ankerite replacement, late-stage dolomitization, and silicification.

Despite the complex post-depositional history, previous studies of the Mosher carbonate have revealed intriguing geochemical signals such as negative Ce-anomalies that could be indicative of an Archean oxygen oases (Fralick and Riding, 2015; Riding et al., 2014). However, the interpretation that these geochemical signals reflect oxygen production (and the early evolution of oxygenic photosynthesis) is disputed due to the degree of post-depositional alteration of the Mosher carbonate (Planavsky et al., 2010). This problem is not unique to the

Mosher carbonate, but applies to all Archean geochemical records that are built from altered billion-year-old rocks (Albut et al., 2018; Bonnand et al., 2020; Heard et al., 2021; Slotznick et al., 2022).

Geochemical analyses

The majority of the samples from the Mosher carbonate were collected during field work in the Steep Rock Lake area in October 2019 (Fig S1). These samples were supplemented by two additional samples collected by Fralick and Riding (SR9-16 and SR8-44) (Fralick and Riding, 2015). All samples were micro-drilled, specifically targeting fabrics and textures that represent the suite of diagenetic end-members from severely recrystallized textures to well-preserved fabrics. The identification of different fabrics in hand-samples was supported by petrographic analysis on thin-sections. The thin-sections and matching blocks were later used for Rare Earth Element and yttrium analysis by laser-ablation ICP-MS (see methods below).

In preparation for geochemical analysis, the micro-drilled carbonate powder was dissolved in 0.1 N acetic acid buffered by ammonium hydroxide (pH of ~5). The solution was placed in a 15 mL Falcon centrifuge tube and allowed to react in an ultra-sonicator for 4 hours. This procedure readily dissolves limestone and dolomite, but leaves less soluble sediment components unreacted, such as Fe-Mn oxides and clays (Husson et al., 2015). Each solution was centrifuged at 2500 rpm for 30 mins before pipetting the upper 3 mL of supernatant into a new Falcon tube that had been pre-rinsed in MilliQ water. This supernatant was used for measurements of Ca isotopes, Sr/(Ca+Mg), and Mn/(Ca+Mg) ratios as detailed below.

C and O isotope analysis, IRMS

Stable carbon ($\delta^{13}\text{C}$) and oxygen ($\delta^{18}\text{O}$) analyses were conducted following established methods at the University of Victoria using a Sercon 20-22 gas-source continuous-flow isotope

ratio mass spectrometer with a GasBox II front end (Lei et al., 2022). Measurements were corrected for instrumental drift by repeated analyses of IAEA standards CO-8 and 603, evenly distributed throughout the runs. The precision of the measurements is evaluated to be 0.18‰ (2σ) from $\delta^{13}\text{C}$ and 0.58‰ (2σ) for $\delta^{18}\text{O}$ based on long-term repeated measurements of an in-house standard (VTS).

Ca isotopes, MC ICP-MS

Calcium was purified from the sample matrix using a Thermo Dionex 5000+ ion chromatography (IC) system following established methods (Husson et al., 2015). To avoid organic contamination, the collected Ca fractions were dried down and treated with concentrated HNO_3 on a hot-plate, before being re-dried and re-dissolve in 2% HNO_3 prior to isotope analysis.

Calcium isotope analyses were performed on a Thermo Neptune Plus MC ICP-MS following methods outlined by previous studies (Husson et al., 2015). Instrumental mass bias drift was corrected using sample-standard bracketing methods with a single-element high-purity Ca standard (HPS) and each sample was measured twice within the same session. In preparation for isotope analysis, all samples were diluted to 2 ppm to match HPS standard concentrations within <5% to ensure comparable levels of Ar-based interference across samples and standards and minimize concentration-dependent isotope effects. Samples were introduced to the mass spectrometer using an ESI Apex-IR sample desolvation system. The analyses were conducted in medium resolution mode, measuring $\delta^{44/42}\text{Ca}$, $\delta^{44/43}\text{Ca}$, and $\delta^{43/42}\text{Ca}$. The ^{42}Ca beam was measured on the low-mass side shoulder of the peak to avoid interference from ArHH. Mass 43.5 was also measured to correct for potential Sr-based interference from doubled charged ^{88}Sr , ^{86}Sr and ^{84}Sr . On average, measurements yielded a mass 44 beam intensity between 2 and 3V. $\delta^{44/42}\text{Ca}_{\text{HPS}}$ values were converted to $\delta^{44/40}\text{Ca}_{\text{seawater}}$ based on two seawater standards measured

within the same runs, assuming that the kinetic isotope mass fractionation law governing the slope between $\delta^{44/40}\text{Ca}$ and $\delta^{44/42}\text{Ca}$ (Gussone et al., 2020). The assumption of kinetic fraction is also supported by the relationship between measurements of $\delta^{44/42}\text{Ca}$ and $\delta^{44/43}\text{Ca}$, which a slope of 0.478 (Fig. S2).

The accuracy of the Ca isotope measurements is evaluated based on the long-term reproducibility of standards; NIST SRM-915b and NIST SRM-915a, yielding values of -1.19 ± 0.14 (2σ , $N=120$) and -1.86 ± 0.16 (2σ , $N=24$), respectively. The 2σ external precision of the measurements in this study is further evaluated using an in-house synthetic aragonite standard, which was taken through the automated column chromatography system and included in every run, yielding values of -1.50 ± 0.19 (2σ , $N=20$).

Major and trace element analysis, ICAP

The Sr/[Ca+Mg] (mmol/mol), Mn/[Ca+Mg] (mmol/mol), and Mg/Ca (mmol/mol) ratios were measured using a Thermo Fischer iCAP Q ICP-MS at Princeton University. The metal ratios were determined using a set of matrix-matched in-house standards spanning the sample concentration range. The external reproducibility of the ratios is estimated within <11%, evaluated from long-term replicate measurements of NIST 240 SRM-88b ($N=92$).

REE+Y analyses, LA ICP-MS

LA-ICP-MS was used to measure the composition of specific micro-fabrics within individual samples. For the petrographic thin-section analysis, samples were embedded in epoxy resin and made into thin-section. For the LA-ICP-MS analyses, the matching sample ‘blocks’ were used, allowing a direct “non-destructive” geochemical comparison to the thin-sections.

Analyses were carried out at the University of Victoria using an integrated in situ Teledyne CETAC LSX-213 G2+ laser ablation system equipped with a HelEx II sample cell and

coupled to an Agilent 8800 #100 ICP-MS/MS. Laser operating conditions and measurement protocols were optimized to obtain maximum precision. The NIST SRM615 and NIST SRM613 glass standards were used to correct for drift and assess accuracy and precision. The detection limit for REE+Y is below 1 ppb and the reproducibility is <10%. The composition of targeted sample fabrics were calculated as the mean composition of a 500 μm long scan with a 100 μm diameter spot. The scan speed was set to 10 $\mu\text{m}/\text{s}$, fluence of 7.14 J/cm^2 , and laser output of 35 with a rep rate of 10 Hz. The instrument parameters and laser energy could not effectively ionize silica and measurements of silicified fabrics were thus not included in the analyses. Each scan took ~ 2 mins; 4 s of dwell time, followed by an initial 40 s acquisition of background signal, followed by a 50 s sample-data acquisition interval, finished by another 30 s of background acquisition.

Calcium was used as an internal standard and the metal to calcium ratio was calibrated from the known metal to calcium ratio of the NIST standards. The total REE concentration in ppm (ug/g) was estimated from the measured REE/Ca and Mg/Ca ratios, assuming that each sample is composed of pure calcite or dolomite end-members with a known molar mass of 100.086 g/mol and 144.399 g/mol, respectively. For comparison to previous studies, REE+Y concentrations were normalized to Post-Archean Australian Shale (McLennan et al., 1980) and different sample microfabrics were plotted for comparison (Fig. S3). Eu and Ce anomalies were calculated following equations from (Heard et al., 2022)

$$Ce/Ce_{SN}^* = \frac{Ce_{SN}}{(Pr_{SN}^{2.571} * Nd_{SN}^{-1.931} * Sm_{SN}^{0.360})}$$

$$Eu/Eu_{SN}^* = \frac{Eu_{SN}}{(Sm_{SN}^{0.5} * Gd_{SN}^{0.5})}$$

REFERENCES CITED

- Albut, G., Babechuk, M.G., Kleinhanns, I.C., Bengler, M., Beukes, N.J., Steinhilber, B., Smith, A.J.B., Kruger, S.J., Schoenberg, R., 2018. Modern rather than Mesoarchean oxidative weathering responsible for the heavy stable Cr isotopic signatures of the 2.95 Ga old Ijzermijn iron formation (South Africa). *Geochim. Cosmochim. Acta* 228, 157–189. <https://doi.org/10.1016/j.gca.2018.02.034>
- Bonnand, P., Lalonde, S.V., Boyet, M., Heubeck, C., Homann, M., Nonnotte, P., Foster, I., Konhauser, K.O., Köhler, I., 2020. Post-depositional REE mobility in a Paleoproterozoic banded iron formation revealed by La-Ce geochronology: A cautionary tale for signals of ancient oxygenation. *Earth Planet. Sci. Lett.* 547, 116452. <https://doi.org/10.1016/j.epsl.2020.116452>
- Fralick, P., Riding, R., 2015. Steep Rock Lake: Sedimentology and geochemistry of an Archean carbonate platform. *Earth-Sci. Rev.* 151, 132–175. <https://doi.org/10.1016/j.earscirev.2015.10.006>
- Gussone, N., Ahm, A.-S.C., Lau, K.V., Bradbury, H.J., 2020. Calcium isotopes in deep time: Potential and limitations. *Chem. Geol.* 544, 119601. <https://doi.org/10.1016/j.chemgeo.2020.119601>
- Heard, A.W., Aarons, S.M., Hofmann, A., He, X., Ireland, T., Bekker, A., Qin, L., Dauphas, N., 2021. Anoxic continental surface weathering recorded by the 2.95 Ga Denny Dalton Paleosol (Pongola Supergroup, South Africa). *Geochim. Cosmochim. Acta* 295, 1–23. <https://doi.org/10.1016/j.gca.2020.12.005>
- Heard, A.W., Bekker, A., Kovalick, A., Tsikos, H., Ireland, T., Dauphas, N., 2022. Oxygen production and rapid iron oxidation in stromatolites immediately predating the Great Oxidation Event. *Earth Planet. Sci. Lett.* 582, 117416. <https://doi.org/10.1016/j.epsl.2022.117416>
- Husson, J.M., Higgins, J.A., Maloof, A.C., Schoene, B., 2015. Ca and Mg isotope constraints on the origin of Earth's deepest $\delta^{13}\text{C}$ excursion. *Geochim. Cosmochim. Acta* 160, 243–266. <https://doi.org/10.1016/j.gca.2015.03.012>
- Lei, J.Z.X., Golding, M.L., Husson, J.M., 2022. Paleoenvironmental interpretation of the Late Triassic Norian – Rhaetian boundary interval in the Whitehorse Trough (Stikine Terrane, northern Canadian Cordillera). *Palaeogeogr. Palaeoclimatol. Palaeoecol.* 608, 111306. <https://doi.org/10.1016/j.palaeo.2022.111306>
- McLennan, S.M., Nance, W.B., Taylor, S.R., 1980. Rare earth element-thorium correlations in sedimentary rocks, and the composition of the continental crust. *Geochim. Cosmochim. Acta* 44, 1833–1839. [https://doi.org/10.1016/0016-7037\(80\)90232-X](https://doi.org/10.1016/0016-7037(80)90232-X)
- Planavsky, N., Bekker, A., Rouxel, O.J., Kamber, B., Hofmann, A., Knudsen, A., Lyons, T.W., 2010. Rare Earth Element and yttrium compositions of Archean and Paleoproterozoic Fe formations revisited: New perspectives on the significance and mechanisms of deposition. *Geochim. Cosmochim. Acta* 74, 6387–6405. <https://doi.org/10.1016/j.gca.2010.07.021>
- Riding, R., Fralick, P., Liang, L., 2014. Identification of an Archean marine oxygen oasis. *Precambrian Res.* 251, 232–237. <https://doi.org/10.1016/j.precamres.2014.06.017>
- Riding, R., Liang, L., Fralick, P., 2022. Oxygen-induced chemocline precipitation between Archean Fe-rich and Fe-poor carbonate seas. *Precambrian Res.* 383, 106902. <https://doi.org/10.1016/j.precamres.2022.106902>

- Slotznick, S.P., Johnson, J.E., Rasmussen, B., Raub, T.D., Webb, S.M., Zi, J.-W., Kirschvink, J.L., Fischer, W.W., 2022. Reexamination of 2.5-Ga “whiff” of oxygen interval points to anoxic ocean before GOE. *Sci. Adv.* 8. <https://doi.org/10.1126/sciadv.abj7190>
- Tomlinson, K.Y., Davis, D.W., Stone, D., Hart, T.R., 2003. U–Pb age and Nd isotopic evidence for Archean terrane development and crustal recycling in the south-central Wabigoon subprovince, Canada. *Contrib. Mineral. Petrol.* 144, 684–702. <https://doi.org/10.1007/s00410-002-0423-0>

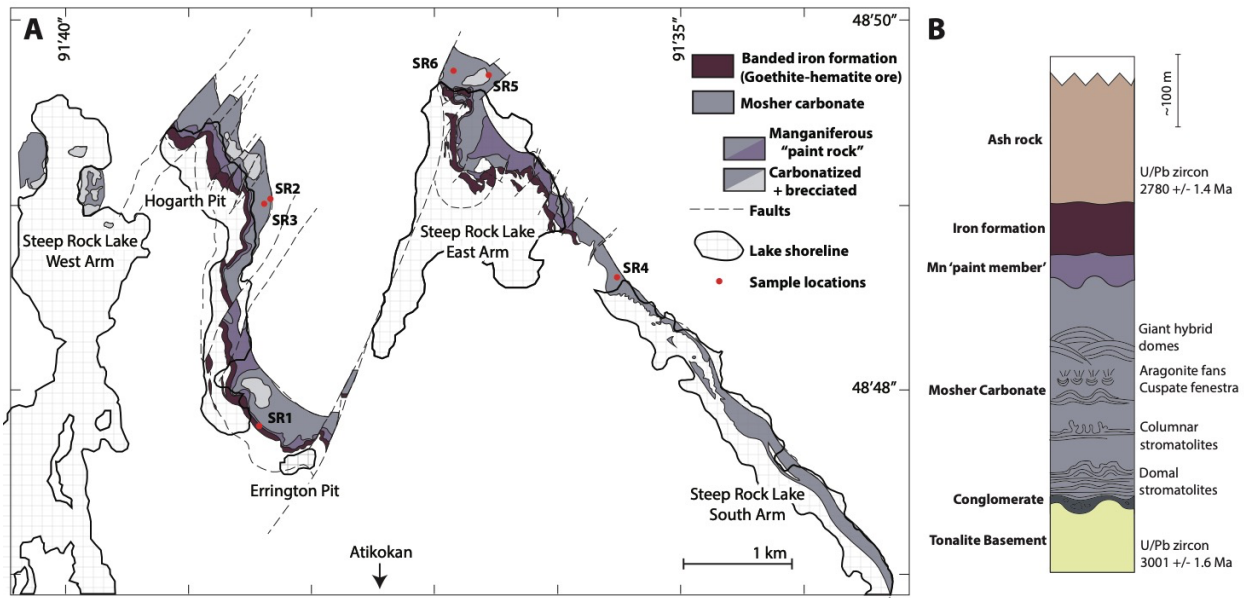


Fig. S1. Geological map of the Steep Rock Lake area and stratigraphic age constraints. (A)

Geological map modified from the original 1972 map by the Ontario Department of Mines and Northern Affairs updated with the current extend of the lake shoreline. Sampling locations are marked in red. **(B)** Stratigraphic column modified from (Fralick and Riding, 2015) including age constraints from (Tomlinson et al., 2003).

constraints from (Tomlinson et al., 2003).

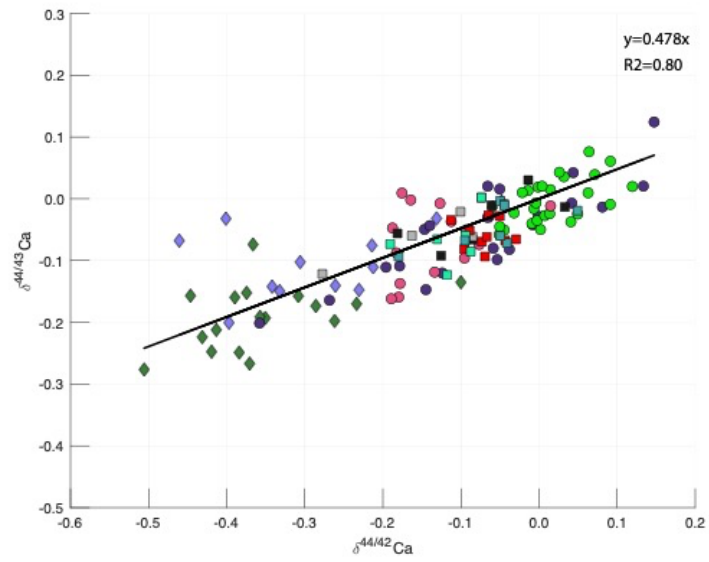


Fig. S2. Mass dependent correlation. Correlation of mass 44/42 and 44/43 confirming mass dependent behavior with a slope of 0.478. Samples are colored according to the legend in Fig. 1.

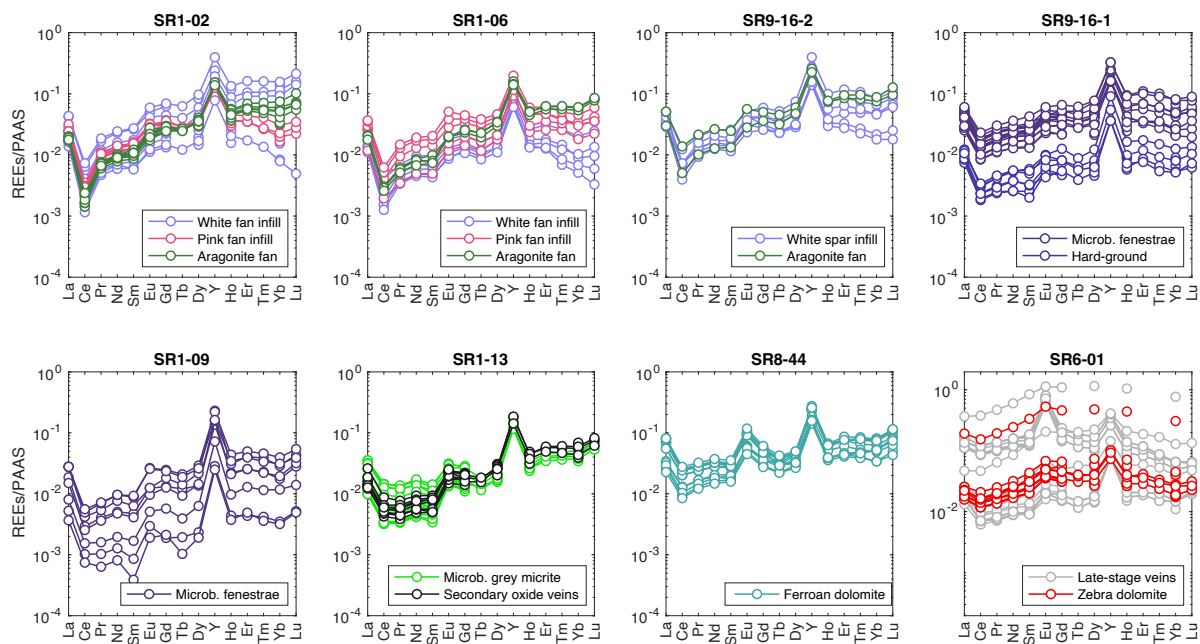


Fig. S3. REE+Y patterns for individual samples. Samples SR1-02, SR1-06, SR9-16-2 are classified as sediment-buffered. Samples SR9-16-1, SR-09, and SR1-13 are classified as fluid-buffered samples. Samples SR8-44 and SR6-01 are classified as being influenced by late-stage alteration.

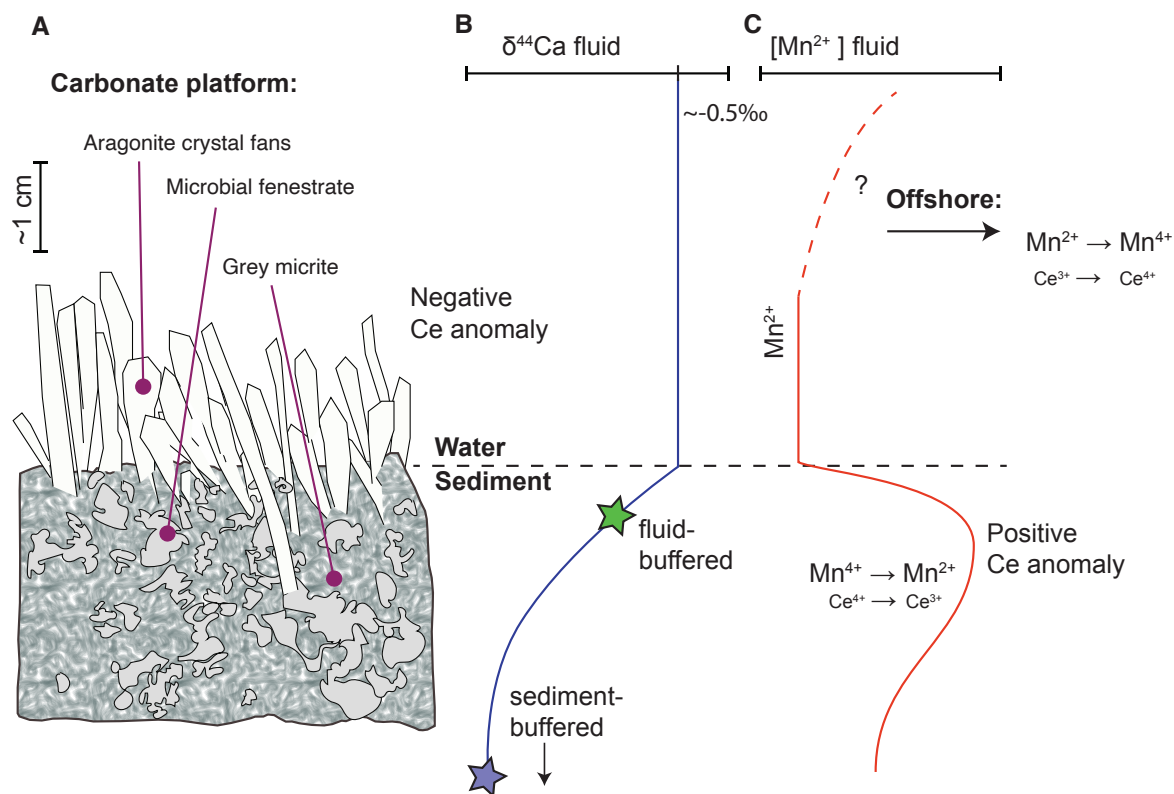


Fig. S4. Conceptual profile of early marine diagenesis in an Archean microbial mat. (A) A schematic of an Archean microbial mat with an open pore framework (microbial fenestrae) and aragonite crystal fans growing above the sediment-water interface. (B) A profile of reconstructed $\delta^{44}\text{Ca}$ fluid values going from the water column and through the microbial mat. During early diagenesis, carbonate cements precipitate in the pore-space, forming microbial fenestrae with seawater-buffered $\delta^{44}\text{Ca}$ values (high fluid-rock ratio). Aragonite recrystallization occurs at depth in a sediment-buffered system (low fluid-rock ratio) at intermediate-stage burial. (C) A profile of reconstructed Mn^{2+} concentrations. The water-column has relatively low Mn^{2+} concentrations, resulting from the formation of Mn-oxides offshore (Fralick and Riding, 2015), while the pore-fluids have higher Mn^{2+} concentrations resulting from the reductive dissolution of Mn-oxides. The precipitation of Mn oxides offshore also resulted in the simultaneous removal of

Ce. This process lowered the Ce³⁺ content of seawater resulting in negative Ce anomalies in the pseudomorph fans (Fralick and Riding, 2015; Riding et al., 2014). In contrast, the reduction and mobilization of Ce in the sediment resulted in positive Ce anomalies recorded in some microbial fenestrae (Riding et al., 2022).

Data S1. (separate file)

Excel file containing all geochemical data